



First Results from the JWST Early Release Science Program Q3D: The Warm Ionized Gas Outflow in $z \sim 1.6$ Quasar XID 2028 and Its Impact on the Host Galaxy

Sylvain Veilleux¹ , Weizhe Liu² , Andrey Vayner³ , Dominika Wylezalek⁴ , David S. N. Rupke⁵ , Nadia L. Zakamska^{3,6} , Yuzo Ishikawa³ , Caroline Bertemes⁴ , Jorge K. Barrera-Ballesteros⁷ , Hsiao-Wen Chen⁸ , Nadiia Diachenko⁹ , Andy D. Goulding¹⁰ , Jenny E. Greene¹⁰ , Kevin N. Hainline¹¹ , Fred Hamann¹² , Timothy Heckman³ , Sean D. Johnson¹³ , Hui Xian Grace Lim⁵ , Dieter Lutz¹⁴ , Nora Lützgendorf¹⁵ , Vincenzo Mainieri¹⁶ , Roberto Maiolino^{17,18} , Ryan McCrory⁵ , Grey Murphree^{5,19} , Nicole P. H. Nesvadba²⁰ , Patrick Ogle²¹ , Swetha Sankar⁹ , Eckhard Sturm¹⁴ , and Lillian Whitesell⁵

¹ Department of Astronomy and Joint Space-Science Institute, University of Maryland, College Park, MD 20742, USA; oscarlwz@gmail.com

² Department of Astronomy, Steward Observatory, University of Arizona, Tucson, AZ 85719, USA

³ Department of Physics and Astronomy, Bloomberg Center, Johns Hopkins University, Baltimore, MD 21218, USA

⁴ Zentrum für Astronomie der Universität Heidelberg, Astronomisches Rechen-Institut, Mönchhofstraße 12-14, D-69120 Heidelberg, Germany

⁵ Department of Physics, Rhodes College, Memphis, TN 38112, USA

⁶ Institute for Advanced Study, Princeton, NJ 08540, USA

⁷ Instituto de Astronomía, Universidad Nacional Autónoma de México, AP 70-264, CDMX 04510, Mexico

⁸ Department of Astronomy & Astrophysics, The University of Chicago, 5640 South Ellis Avenue, Chicago, IL 60637, USA

⁹ Department of Physics and Astronomy, Bloomberg Center, Johns Hopkins University, 3400 North Charles Street, Baltimore, MD 21218, USA

¹⁰ Department of Astrophysical Sciences, Princeton University, 4 Ivy Lane, Princeton, NJ 08544, USA

¹¹ Steward Observatory, University of Arizona, 933 North Cherry Avenue, Tucson, AZ 85721, USA

¹² Department of Physics & Astronomy, University of California, Riverside, CA 92521, USA

¹³ Department of Astronomy, University of Michigan, Ann Arbor, MI 48109, USA

¹⁴ Max-Planck-Institut für Extraterrestrische Physik, Giessenbachstrasse 1, D-85748 Garching, Germany

¹⁵ European Space Agency, Space Telescope Science Institute, Baltimore, MD 21218, USA

¹⁶ European Southern Observatory, Karl-Schwarzschild-Straße 2, D-85748 Garching bei München, Germany

¹⁷ Kavli Institute for Cosmology, University of Cambridge, Cambridge, CB3 0HE, UK

¹⁸ Cavendish Laboratory, University of Cambridge, Cambridge, CB3 0HE, UK

¹⁹ Institute for Astronomy, University of Hawai'i, Honolulu, HI 96822, USA

²⁰ Université de la Côte d'Azur, Observatoire de la Côte d'Azur, CNRS, Laboratoire Lagrange, Bd de l'Observatoire, CS 34229, Nice cedex 4 F-06304, France

²¹ Space Telescope Science Institute, 3700, San Martin Drive, Baltimore, MD 21218, USA

Received 2023 March 15; revised 2023 May 31; accepted 2023 June 18; published 2023 August 2

Abstract

Quasar feedback may regulate the growth of supermassive black holes, quench coeval star formation, and impact galaxy morphology and the circumgalactic medium. However, direct evidence for quasar feedback in action at the epoch of peak black hole accretion at $z \approx 2$ remains elusive. A good case in point is the $z = 1.6$ quasar WISEA J100211.29+013706.7 (XID 2028), where past analyses of the same ground-based data have come to different conclusions. Here, we revisit this object with the integral-field unit of the Near Infrared Spectrograph on board the JWST as part of Early Release Science program Q3D. The excellent angular resolution and sensitivity of the JWST data reveal new morphological and kinematic substructures in the outflowing gas plume. An analysis of the emission-line ratios indicates that photoionization by the central quasar dominates the ionization state of the gas with no obvious sign for a major contribution from hot young stars anywhere in the host galaxy. The rest-frame near-UV emission aligned along the wide-angle cone of outflowing gas is interpreted as a scattering cone. The outflow has cleared a channel in the dusty host galaxy, through which some of the quasar ionizing radiation is able to escape and heat the surrounding interstellar and circumgalactic media. Although the warm ionized outflow is not powerful enough to impact the host galaxy via mechanical feedback, radiative feedback by the active galactic nucleus, aided by the outflow, may help to explain the unusually small molecular gas mass fraction in the galaxy host.

Unified Astronomy Thesaurus concepts: Galaxy winds (626); Quasars (1319); Active galaxies (17); AGN host galaxies (2017)

1. Introduction

Cosmological galaxy formation simulations have long pointed to the need for feedback processes that regulate the growth of galaxies and their central supermassive black holes (SMBHs) to reproduce the observed galaxy morphological types and mass function (e.g., Benson et al. 2003; Nelson et al. 2019;

Oppenheimer et al. 2020), the tight relation between SMBHs and the spheroids hosting them (e.g., Gebhardt et al. 2000; Gültekin et al. 2009; Hopkins et al. 2016), and the properties of the circumgalactic medium (CGM; Tumlinson et al. 2017). These processes fall into two broad categories: external processes associated with the environment (e.g., ram-pressure and tidal stripping, evaporation, harassment, and halo quenching, predominantly taking place in rich galaxy clusters) and internal processes driven from within the galaxies (e.g., energy released from stellar processes or gas accretion onto SMBHs powering active galactic nuclei (AGNs) or luminous quasars).



Original content from this work may be used under the terms of the [Creative Commons Attribution 4.0 licence](https://creativecommons.org/licenses/by/4.0/). Any further distribution of this work must maintain attribution to the author(s) and the title of the work, journal citation and DOI.

Cosmological simulations suggest that energy released from stellar feedback alone is capable of reproducing the properties of galaxies with stellar masses smaller than $\sim 3 \times 10^{11} M_{\odot}$, although observational evidence has grown in recent years to show that AGN feedback may also play a supporting role in at least some dwarf galaxies (Koudmani et al. 2019; Manzano-King et al. 2019; Liu et al. 2020; Koudmani et al. 2021, 2022). Meanwhile, larger galaxies with stellar masses above $\sim 3 \times 10^{11} M_{\odot}$ require energy that is well in excess of that available from stellar processes, so AGN feedback is invoked as the dominant driver in these systems. AGN feedback has also been invoked to explain the observed rapid ($\lesssim 10^9$ yr) inside-out cessation (quenching) of star formation in some massive galaxies (Schawinski et al. 2014; Onodera et al. 2015; Tacchella et al. 2015, 2016; Spilker et al. 2019).

Feedback specifically associated with AGNs comes in two flavors: (i) the “kinetic” or “radio” mode, where the energy from light relativistic jets produced in slowly accreting and radiatively inefficient AGNs with Eddington ratios $L_{\text{AGN}}/L_{\text{Edd}} \lesssim 10^{-3}$ (e.g., Yuan & Narayan 2014) couple with the environment to prevent the gas from forming stars efficiently, or (ii) the “radiative” or “quasar” mode, in which the radiation from luminous fast-accreting AGNs with $L_{\text{AGN}}/L_{\text{Edd}} > 10^{-3}$ heats or ionizes the surrounding gas (radiative feedback) or exerts a force that stirs up or ejects gas out of the galaxy and into the CGM or intergalactic medium (IGM) before it is able to form stars (mechanical feedback).

There is growing observational support for both flavors of AGN feedback. Some of the most dramatic examples of AGN feedback in action are found in the central regions of cool-core galaxy clusters, where mechanical heating by the central jetted AGN almost perfectly offsets radiative cooling of the hot intracluster medium (ICM; e.g., McNamara & Nulsen 2007; Fabian 2012). This radio-mode feedback also acts on galactic scales where the relativistic jets of radio galaxies deposit part of their energy into the interstellar medium (ISM) of the host galaxies, stirring up the cool gas that would otherwise be forming stars (preventive feedback; e.g., Dasyra et al. 2015, 2016; Nesvadba et al. 2021), and driving in some cases strong outflows where the entrained material is ejected into the CGM (ejective feedback; e.g., Nesvadba et al. 2008, 2010, 2017; Li et al. 2021).

Direct observational evidence for quasar-mode negative feedback has also grown over the years. Radiative feedback is observed in several powerful AGNs and quasars, where the ionizing radiation alters the physical state of the gas in the host galaxy and its CGM (e.g., Howell et al. 2007; Curran & Whiting 2012; Kreimeyer & Veilleux 2013; Borisova et al. 2016; Johnson et al. 2018; Arrigoni Battaia et al. 2019; Farina et al. 2019; Helton et al. 2021), companion galaxies in the proximity of the quasar (e.g., Francis & Bland-Hawthorn 2004; Bruns et al. 2012), and sometimes much beyond (proximity effect on Mpc scales; e.g., Bajtlik et al. 1988; Gonçalves et al. 2008; Eilers et al. 2020; Morey et al. 2021, and references therein).

Mechanical feedback in the form of galaxy-scale outflows has also been detected and mapped using integral-field spectroscopy (IFS) in several local galaxies and a growing number of distant quasars (see reviews by, e.g., Ciccone et al. 2018; Harrison et al. 2018; Rupke 2018; Veilleux et al. 2020, and references therein). The large energetics of the entrained material suggest that these outflow episodes are life-altering

events for the host galaxies, although the uncertainties on the duty cycle and full extent of these outflows make it difficult to assess the long-term impact of these outflows on the evolution of the galaxy hosts and their environments. Moreover, in some cases, AGN-driven outflows may instead trigger (positive feedback), rather than suppress (negative feedback), new star formation by compressing the ambient gas in the host galaxy (e.g., Croft et al. 2006; Elbaz et al. 2009; Cresci et al. 2015; Shin et al. 2019). In situ star formation may also be taking place within the outflowing gas itself in cases of heavily mass-loaded outflows (e.g., Maiolino et al. 2017; Gallagher et al. 2019; Rodríguez del Pino et al. 2019).

The fastest and most powerful winds are found in rapidly accreting luminous quasars, hence they are the best laboratories to study quasar feedback. These quasars are more common at the epoch of peak SMBH accretion around cosmic noon ($z \sim 2$), but their large distances make them challenging to study in detail with ground-based facilities. Our current understanding of quasar-mode feedback, and feedback in general, has so far been limited by the modest IR sensitivity, angular resolution, and quality of the PSF characterization of ground-based IFS facilities. The integral-field spectrographs on board the JWST (Gardner et al. 2006) have opened a new window on the high- z Universe, and quasar feedback in particular.

As part of the Director’s Discretionary Early Release Science program Q3D (PID 1335, PI Wylezalek, co-PIs Veilleux, Zakamska; Software Lead: Rupke), three luminous obscured quasars were observed in the IFS mode of the Near Infrared Spectrograph (NIRSpec; Jakobsen et al. 2022). The first results on the $z \sim 3$ quasar SDSS J165202.64+172852.3 (J1652 for short) were presented in Wylezalek et al. (2022), followed by more detailed analyses in Vayner et al. (2023, submitted). In the present paper, we discuss the results of the first-look analysis of the NIRSpec IFS data on the $z = 1.6$ quasar WISEA J100211.29+013706.7 (XID 2028 hereafter).

XID 2028 is a prototypical obscured quasar. It was specifically selected from the XMM-Newton-COSMOS survey (Hasinger et al. 2007) on the basis of its observed red color ($r - K = 4.81$) and high X-ray to optical flux ratio ($f_{2-10 \text{ keV}}/f_{r\text{-band}}^{23} > 10$; Brusa et al. 2010). Over the years, this object has become a prime target to study quasar feedback in action. Evidence for both negative and positive feedback has been reported in this object based on the results of analyses of ground-based long-slit and integral-field spectroscopic data on the rest-frame optical emission lines (Brusa et al. 2015; Cresci et al. 2015; Perna et al. 2015) and at millimeter waves with the Atacama Large Millimeter/submillimeter Array (ALMA; Brusa et al. 2018). However, a recent reanalysis of the same rest-frame optical IFS data found no evidence for suppressed or enhanced star formation due to the outflow in this object (Scholtz et al. 2020). These authors discussed the possibility that the different conclusions may be due to different intermediate data reduction steps (e.g., sky subtraction or frame stacking).

The main objectives of this first paper on the JWST data of XID 2028 are to characterize the warm ionized outflow in this system, and assess the impact of the outflow and quasar radiation field on the host galaxy. This paper is organized as follows. In Section 2, we describe the observations and steps

²³ The r -band flux was computed by Brusa et al. (2010) by converting the r -band magnitude into a monochromatic flux and then multiplying the results by the width of the r -band filter.

taken to reduce the JWST data. Our use of the software package `q3dfit` to analyze these data is discussed in Section 3. We present the results from this analysis in Section 4. We discuss the properties of the outflow and impact of this outflow on the host galaxy in the context of quasar feedback scenarios in Section 5, taking into account the large set of ancillary data on this object. The conclusions are summarized in Section 6.

Throughout this paper, we assume the same Lambda cold dark matter (Λ CDM) cosmology as in Wylezalek et al. (2022): $H_0 = 70 \text{ km s}^{-1} \text{ Mpc}^{-1}$, $\Omega_m = 0.3$, and $\Omega_\Lambda = 0.7$. The resulting luminosity distance and physical scale is 11.751 Gpc and $1'' = 8.471 \text{ kpc}$, respectively, given the redshift of XID 2028 derived from our data ($z = 1.5933$; Section 4.2). All emission lines are identified by their wavelength in air (e.g., [O III] $\lambda 5007$), but all wavelength measurements are performed on the vacuum wavelength scale.

2. Observations and Data Reduction

2.1. Observations

XID 2028 was observed on 2022 November 20 by JWST using the NIRSpec Instrument in IFU mode (Böker et al. 2022; Jakobsen et al. 2022). These data are publicly available on the Mikulski Archive for Space Telescopes (MAST) at the Space Telescope Science Institute. The specific observations analyzed can be accessed via doi:10.17909/04tb-mn90. The NIRSpec field of view (FOV) in IFU mode is $\sim 3'' \times 3''$ or $\sim 25 \times 25 \text{ kpc}$ for this object. We used the filter/grating combination F100LP/G140H, with corresponding wavelength coverage of $0.97\text{--}1.89 \mu\text{m}$ or $\sim 0.37\text{--}0.73 \mu\text{m}$ at the redshift of XID 2028. The grating has a near-constant dispersion $\Delta\lambda = (2.30 - 2.40) \times 10^{-4} \mu\text{m}$ per pixel, corresponding to a velocity resolution $\sim 80\text{--}180 \text{ km s}^{-1}$. This allows us to easily spectrally resolve the profiles of the emission lines in XID 2028, which have typical velocity widths of several hundred km s^{-1} . As in the case of the J1652 observations (Wylezalek et al. 2022), we used a nine-point small cycling dither pattern with 25 groups and one integration per position to improve the spatial sampling, and help us more accurately measure and characterize the point-spread function (PSF). We also took one leakage exposure at the first dither position to account for light leaking through the closed microshutter array (MSA), as well as light from failed open shutters. Following the recommendation of the STScI staff, we used the NRSIRS2 readout mode, which improves the signal-to-noise ratio and reduces data volume compared to the NRSIR2RAPID mode. No pointing verification image was taken. The total integration time was 177 minutes on target and 20 minutes for the leakage exposure.

2.2. Data Reduction

The NIRSpec data of XID 2028 were reduced following largely the same method used by Vayner et al. (2023, submitted) to reduce the NIRSpec data cube on J1652. We refer the interested reader to this paper for more details. Here, we describe the main steps with an emphasis on aspects that are specific to the NIRSpec data on XID 2028.

Data reduction was done with the JWST Calibration pipeline version 1.8.4 (Bushouse et al. 2022) using CRDS version 11.16.16 and context file `jwst_1019.pmap`. The first stage of the pipeline, `Detector1Pipeline`, performs standard IR detector reduction steps, such as dark current subtraction,

fitting ramps of non-destructive group readouts, combining groups and integrations, data quality flagging, cosmic ray removal, bias subtraction, linearity, and persistence correction.

Afterward, we ran `Spec2Pipeline`, which assigns a world coordinate system to each frame, applies flat field correction, flux calibration, and extracts the 2D spectra into a 3D data cube using the `cube build` routine. Here, we adopt the `emsm` weighting method instead of the standard drizzle method to build the 3D data cube from the 2D data.²⁴ The `emsm` weighting reduced the oscillating spectral pattern in the point-source spectrum compared to the drizzle method at the cost of minor degradation in the spatial and spectral resolution. Additional steps were taken to flag pixels affected by open MSA shutters. At this point, we skipped the imprint subtraction step due to increased spatial variation in the background across many spectral channels. Due to known issues with the outlier detection step in the `Spec3Pipeline` (JWST Help Desk, priv. communication), we opted to use the `reproject` package²⁵ to combine the different dither positions into a single data cube using their drizzle algorithm. The dither positions were combined onto a common grid with a spatial pixel size of $0''.05$.

The astrometry of the cube obtained by the JWST Calibration pipeline features a minor offset with respect to archival Hubble Space Telescope (HST) data. We use the position of the quasar in the HST WFC3 F814W image, previously discussed in Brusa et al. (2010, 2015, 2018) and Scholtz et al. (2020), to align the astrometry of the JWST data with respect to the HST image. We find a small offset of $\Delta\text{R.A.} = -0''.07$ and $\Delta\text{decl.} = 0''.03$.

The data cube produced by the pipeline was put on an absolute flux scale by using the data on flux standard star TYC 4433-1800-1 (PID 1128, o009) reduced in exactly the same way as the data cube of XID 2028.

3. Data Analysis

We are interested in the faint extended emission outside of the quasar. Therefore, we need to carefully remove the bright quasar light from the NIRSpec data cube. For this delicate task, we use `q3dfit`²⁶ (D. S. N. Rupke et al. 2023, in preparation), which is a dedicated software package for the removal of bright point-spread function (PSF) from JWST data cubes. `q3dfit` is a Python-based software adapted from `IFSFit` (Rupke 2014; Rupke et al. 2017), which is an IDL-based software which has been used extensively on ground-based IFS data. The major strength of `q3dfit` is that it takes advantage of all of the available spectral information to reconstruct and subtract the PSF with very few priors. The only necessary condition is that the PSF must be sufficiently spectrally different from the extended emission. It is precisely this difference that allows us to identify the PSF without prior knowledge of its spatial shape and spectral dependence.

Our use of `q3dfit` on the NIRSpec data of XID 2028 follows that of the NIRSpec cube of J1652 by Vayner et al. (2023, submitted). We refer the interested reader to this paper for more details. Here, we briefly describe the general philosophy of `q3dfit` and the key aspects relevant to the

²⁴ https://jwst-pipeline.readthedocs.io/en/latest/jwst/cube_build/main.html##algorithm

²⁵ <https://reproject.readthedocs.io/en/stable/>

²⁶ <https://q3dfit.readthedocs.io/en/latest/>

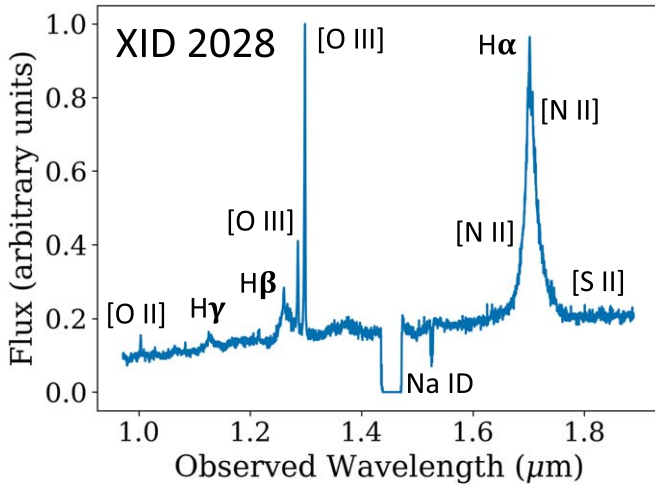


Figure 1. Spectrum of quasar XID 2028 extracted with a circular aperture with a radius of $0''.05$. This spectrum is used as the PSF spectral model in *q3dfit* to remove the quasar light in the NIRSpect cube. The Na I D label indicates the spatially unresolved neutral outflow traced by the Na I 5890, 5896 doublet absorption feature in this quasar.

NIRSpect data on XID 2028. *q3dfit* extracts the quasar spectrum using the brightest spaxels. This quasar spectrum is used as the PSF spectral model. It is scaled across the data cube and then subtracted to reveal the faint extended emission. In this first iteration, the extended emission is fitted with a combination of emission lines, absorption lines, and simple featureless monotonic continuum models. This first fit to the residuals is then used as an input for a second iteration of the quasar spectrum extraction. In this second iteration, the fit to the residuals may be improved by using more sophisticated continuum models, such as galaxy stellar population synthesis (SPS) models, if the data quality justifies it. Similarly, additional iterations on the PSF subtraction and fit of the residuals may be needed to come to stable converging results. While there have been a few other attempts to perform PSF subtraction in IFU data based on this principle (e.g., Husemann +13), *q3dfit* is unique in its ability to conduct iterative fitting of quasar PSF, gas emission, and galaxy stellar population synthesis (SPS) models.

In this first-look paper on XID 2028, we focus on the properties of the extended line emission. No attempt is made to fit the continuum emission with SPS models because the underlying stellar continuum from the host galaxy is faint and the strengths of the emission lines in the extended nebula are unaffected by the stellar features. Each spaxel n is fitted with the sum of the scaled quasar spectrum, a starlight model, and emission lines. Following the nomenclature of Rupke et al. (2017), this can be written as $I^n = I^n_{\text{quasar}} + I^n_{\text{starlight,exp. model}} + I^n_{\text{emission}}$, where the second term on the righthand side is a sum of four featureless monotonic exponential functions. The quasar spectrum, shown in Figure 1, is extracted from the cube using a circular aperture with a radius of $0''.05$ (one spatial pixel), which minimizes the aperture footprint while providing a high-S/N quasar spectrum (the results on the extended nebula described below are unchanged if we use a radius of $0''.1$). In the end, we find that all of the emission-line profiles in XID 2028, after quasar removal, can be fitted adequately with only one or two Gaussian components. These Gaussian components are kinematically locked (same velocity centroids and widths) for all the lines, although their relative strengths are allowed to vary (Figures 2(c)–(f)). This physically motivated

assumption that the ionized gas from different species should have roughly the same kinematics improves the quality of the fits by reducing the dimension of the parameter space of the nonlinear least-square minimization between the fits and data. We do not attribute a physical meaning to the individual Gaussian components (contrary to Cresci et al. 2015). Consequently, in the remainder of this paper, we only show the results derived from the sum of these components, i.e., the integrated line profiles. The wings of the QSO PSF extends to at least $1''$ from the quasar, so our use of *q3dfit* to remove both the continuum and line emission from the central quasar is critical to accurately determine the morphology and detailed line profiles of the faint extended line emission in this object. The residual starlight continuum from the host galaxy is highly nucleated around the quasar. There is no evidence for galaxy companions within ~ 15 kpc of XID 2028 (contrary to J1652; Wylezalek et al. 2022).

4. Results

4.1. [O III] Morphology

[O III] 5007 Å is the strongest emission line in the NIRSpect data cube, as expected from the published ground-based data, and therefore the best tracer of the warm ionized gas in XID 2028; which is the focus of the present section. The *q3dfit* analysis is restricted to 3860–5400 Å in the quasar rest frame to allow us to fit H β , [O III] 4959, 5007 simultaneously, as well as the underlying continuum emission from the quasar and galaxy host.

Figure 3 shows the quasar-subtracted narrowband images of the [O III] 5007 line emission produced by extracting the [O III] 5007 flux from the *q3dfit*-processed data cube across the velocity ranges of $[-1200, -300]$ km s $^{-1}$, $[-300, +300]$ km s $^{-1}$, and $[+300, +500]$ km s $^{-1}$ relative to the quasar rest frame (the systemic velocity of XID 2028, $z = 1.5933$, is derived from our kinematic analysis of the *q3dfit*-processed data cube, discussed in Section 4.2). Figure 3 shows that nearly all the [O III] line-emitting gas outside of the unresolved quasar lies either in a bright western plume of gas with negative radial velocities down to -1000 km s $^{-1}$ (90-percentile) or in fainter blueshifted gas clouds that surround the bright plume and trace a wide-angle cone with an opening angle $\phi \sim 90^\circ$. The line emission extends to the western edge of the field of view of NIRSpect, i.e., at least 17 kpc from the quasar.

As we will discuss later in Section 4.2, the measured negative velocities of the gas are well in excess of those expected for rotational motion in the host galaxy. Therefore, the NIRSpect data nicely confirm the presence of a one-sided fast [O III] outflow in XID 2028, which was first reported by Cresci et al. (2015) and Perna et al. (2015), and was more recently reported by Scholtz et al. (2020), based on independent analyses of ground-based Xshooter and SINFONI IFS data. The improved angular resolution, PSF characterization, and sensitivity of the JWST data reveal intricate bubble-like substructures in the bright plume that were not evident in the ground-based data and resolves outflowing gas clouds, which trace a cone with a wider opening angle than previously suspected. The absence of a redshifted counterpart to the outflow, now confirmed by the NIRSpect data down to a $3\sigma f_\lambda$ limit of 1.4×10^{-20} erg s $^{-1}$ cm $^{-2}$ Å $^{-1}$ arcsec $^{-2}$, combined with the small extent ($R \approx 0''.5 = 4$ kpc) of the near-systemic (± 300 km s $^{-1}$) line emission from the host ISM, puts strong

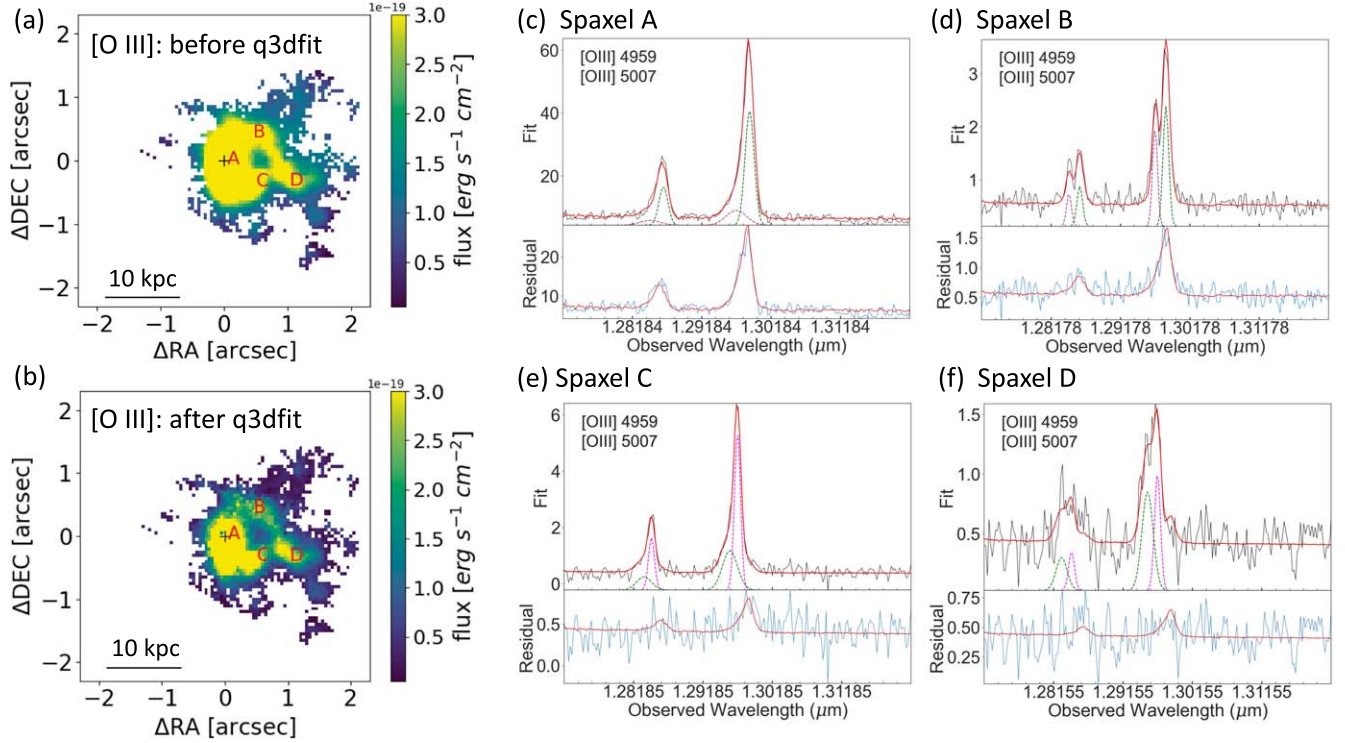


Figure 2. (a) Map of the [O III] 5007 line-emitting nebula before subtraction of the quasar light and galaxy continuum. North is up and east is to the lefthand side. The coordinate system is centered on the quasar position (black cross). The image is ~ 34 kpc on the side. The fluxes are per spaxel ($0''.05 \times 0''.05$). (b) Same as (a) after processing with *q3dfit*. The continuum and line emission from the quasar and the continuum from the host galaxy have been carefully subtracted from this image using *q3dfit* to isolate the extended [O III] line-emitting gas. (c)–(f). Representative spectra centered on [O III] 4959 and 5007 extracted from various spaxels in the [O III] nebula, as indicated in panels (a) and (b). In each panel, the top plot shows the data in black, the fits in red, and the individual Gaussian components of the fit in green and purple. The bottom plot shows the difference between the data and the best-fit host emission lines in blue. The red line is the sum of the scaled quasar spectrum and host continuum modeled with monotonic polynomial functions ($= I_{\text{quasar}}^n + I_{\text{starlight,exp. model}}^n$; see Section 3 for more detail).

constraints on the outflow geometry. We return to this issue in Section 5.

4.2. [O III] Kinematics

The kinematics of the [O III]-emitting gas derived from our *q3dfit* analysis of the data cube centered around $\text{H}\beta$ –[O III] 5007 are shown in Figure 4. The 50-percentile (median, v_{50}) and 90-percentile velocities (v_{90}) are, respectively, the velocities at 50% and 90% of the total [O III] flux, calculated starting from the red side of the line profile. The v_{50} and v_{90} velocity fields in Figure 4 highlight the fact that most of the gas outside of the inner arcsecond region (projected distances $R \gtrsim 4$ kpc from the quasar) is significantly blueshifted with respect to the systemic velocity of the system ($z = 1.5933$), derived from the median velocity, v_{50} , of the line emission in the central arcsecond region (after removal of the quasar light with *q3dfit*). This redshift is consistent within the errors with published values derived from other optical and ALMA data, $z = 1.5930$ (Cresci et al. 2015; Brusa et al. 2018).

A velocity gradient spanning the range $\sim [-250, +250] \text{ km s}^{-1}$ along $\text{PA} = -10^\circ$ is seen in the inner arcsecond ($R \lesssim 4$ kpc) of the nebula centered on the quasar position (Figure 4(a)). This gradient is largely consistent in direction, amplitude, and location with the gradient of the molecular disk detected in the ALMA data (Brusa et al. 2018), which is attributed to galactic rotation in the potential of the host galaxy. The implied circular velocity ($\sim 400 \text{ km s}^{-1}$, assuming that the inclination of the host galaxy disk is the same as that of the

molecular disk, $i = 30^\circ$; Brusa et al. 2018) is consistent with that estimated from the stellar mass of this galaxy: $v_{\text{circ}} = \sqrt{2}S \approx 400 \text{ km s}^{-1}$, where $\log S = 0.29 \log M_* - 0.93$ (Weiner et al. 2006; Kassin et al. 2007) and a stellar mass $\log M_*/M_\odot = 11.65^{+0.35}_{-0.35}$ is used for XID 2028 (Brusa et al. 2018). Therefore, the observed blueshifted velocities in the outer nebula are well in excess of the rotation velocity and are indicative of a large-scale outflow along our line of sight.

Figure 4 also shows velocity gradients on larger scales, along and perpendicular to the bright plume. The gas along the plume is systematically more blueshifted with increasing distance from the quasar: v_{50} (v_{90}) range from ~ -200 (-500) km s^{-1} within ~ 1 – 2 kpc of the quasar to -800 (-1000) km s^{-1} at a distance of 17 kpc. Meanwhile, the gas near the central axis of the plume is systematically more blueshifted by 200 – 300 km s^{-1} than the off-axis gas.

The 80-percentile line widths (defined as $w_{80} = v_{10} - v_{90}$ using the same convention as above to calculate v_{10}) are shown in Figure 4(c). The measured values of w_{80} near the quasar are on average broader by ~ 200 – 300 km s^{-1} than those further out (recall that the quasar light has been scaled and removed here, so it does not contribute to the observed line broadening). Clear line splitting is seen on the northern and southern edges of the bright outflow plume, where both blueshifted and systemic-velocity gas is detected, which is apparent in Figures 2(d), and 3(a) and (b). On average, the [O III] line profiles outside of the plume are slightly narrower by ~ 100 – 200 km s^{-1} than those in the plume.

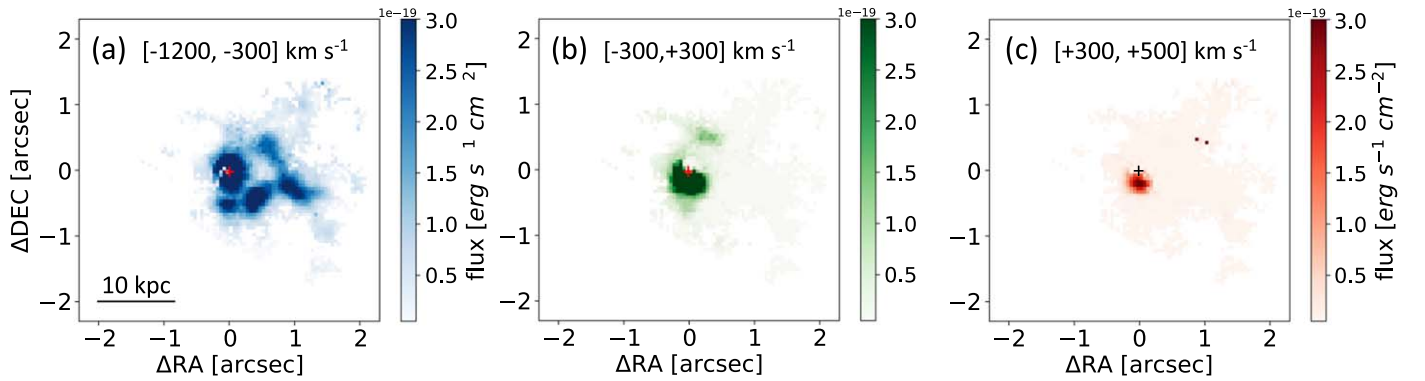


Figure 3. Pseudo-narrowband images, derived from the NIRSpec cube after processing with *q3dfit*, centered on the [O III] 5007 Å emission line at velocities of (a) $[-1200, -300]$ km s $^{-1}$, (b) $[-300, +300]$ km s $^{-1}$, and (c) $[+300, +500]$ km s $^{-1}$. These images are on the same spatial scale and orientation as Figures 2(a) and (b). The continuum and line emission from the quasar and the continuum from the host galaxy have been carefully subtracted from all these images to isolate the extended [O III] line-emitting gas using *q3dfit*. Panel (a) reveals a complex plume of blueshifted gas that is flowing out of the host galaxy at velocities of up to -1000 km s $^{-1}$ (90-percentile) and extends westward out to at least 17 kpc from the quasar. Fainter outflowing gas clouds are also detected around the plume, tracing a wider cone with opening angle $\phi \sim 90^\circ$. The absence of highly redshifted material in panel (c) suggests that the [O III] outflow is either one-sided or the receding counterpart of the outflow is obstructed by the dusty host galaxy.

4.3. Emission-line Ratios

We ran a separate *q3dfit* analysis of the NIRSpec data cube covering 3860–7200 Å in the quasar rest frame to capture the extranuclear H β , [O III] 4959, 5007, H α , [N II] 6548, 6583, and [S II] 6716, 6731 line emission. The results are shown in Figure 5. This analysis allows us to derive the [O III] 5007/H β , [O III] 5007/H α , [N II] 6583/H α , and [S II] 6716, 6731/H α line ratio maps shown in the top panels of Figure 6. We also derive the H α /H β and [S II] 6716/6731 line ratio maps shown in Figure 7. For this analysis, we fit all the above listed emission lines simultaneously to get a consistent fit across all lines, and thus allow inter-line comparisons. The velocity centroids and widths of the individual Gaussian components are once again kinematically locked but allowed to vary in intensity relative to each other. While this approach is necessary to create self-consistent line ratio maps, it does limit the extent of these line ratio maps to only those spaxels where line emission is detected in both lines of the ratios rather than just [O III] 4959, 5007, as in Section 4.2.

In Figures 6(e)–(f), the line ratios measured in the extranuclear nebula of XID 2028 are displayed in the diagnostics line ratio diagrams of (Baldwin et al. 1981, BPT; Figure 6(e)) and (Veilleux & Osterbrock 1987, VO87; Figure 6(f)) to assess the primary source of ionization of the line-emitting gas. The theoretical and empirical curves of Kewley et al. (2001) and Kauffmann et al. (2003), which separate AGNs from star-forming galaxies in these line ratio diagrams, are shown for comparison. We find that virtually all of the line ratios are consistent with photoionization by the central quasar, regardless of the location in the nebula. A more quantitative statement can be made by measuring the distance to the peak of the AGN branch, D_{AGN} , in the [N II] diagram, following Yuan et al. (2010). We get $D_{\text{AGN}} = 0.7\text{--}1$ for nearly all data points in Figure 6(e), confirming that the AGN is the dominant source of ionization of the nebula. The lack of a significant gradient in the line ratios with distance from the quasar also indicates that the nebula is matter-bounded, i.e., it has no ionization edges. We discuss the implications of these results in Section 5.2.

Note that shock models with photoionized precursors (e.g., Allen et al. 2008) are able to reproduce some of the AGN-like line ratios of the XID 2028 nebula, but the lack of obvious

trends between the line ratios and gas kinematics (v_{50} , v_{90} , w_{80}) outside of the inner arcsecond region of the host galaxy suggests that shock ionization and heating are not important in the nebula of XID 2028, contrary to J1652 (Vayner et al. 2023) and shock-dominated systems (e.g., Veilleux et al. 1995; Allen et al. 1999; Sharp & Bland-Hawthorn 2010; Rich et al. 2011, 2014, 2015; Hinkle et al. 2019, and references therein).

Figure 7(a) displays spatial variations in the $\log(\text{H}\alpha/\text{H}\beta)$ ratios that are suggestive of an extinction gradient across the host and outflow regions, with the inner host galaxy region generally displaying larger H α /H β ratios consistent with $A_V \approx 1.1$ mag, while the median value of A_V across the outer outflow region is 0.52 mag. Note that the H α /H β ratios are available over only a limited area of the [O III] nebula. The measurements are systematically more uncertain in the fainter portion of the nebula dominated by the outflowing gas. To avoid introducing noise bias between the host and outflow regions, we did not apply reddening corrections to the line ratios presented in Figure 6. However, we note that our interpretation of the line ratio maps and diagnostic diagrams is robust to these reddening corrections. This is not surprising because, by design (VO87), these line ratio diagrams involve emission lines that are close in wavelengths, and are therefore insensitive to extinction.

5. Discussion

Our *q3dfit* analysis of the new NIRSpec data cube confirms the presence of the fast outflow in XID 2028, first reported by Brusa et al. (2015), Cresci et al. (2015), and Perna et al. (2015), and recently reexamined by Scholtz et al. (2020). The new data reveal a prominent and highly structured plume that extends westward to the edge of the FOV of the NIRSpec IFU ($\sim 2''$ or ~ 17 kpc from the quasar), which is surrounded by slower gas clouds that trace a one-sided cone with an opening angle of $\sim 90^\circ$. This complex bubble-like and conical morphology is not unusual for galaxy-scale outflows where the dense ISM from the host galaxy is being accelerated by a fast AGN wind (e.g., Veilleux et al. 1994; Cecil et al. 2001; Veilleux et al. 2001; Cecil et al. 2002; Greene et al. 2012). In this section, we revisit the energetics and possible driving mechanisms of the outflow by taking into account these new

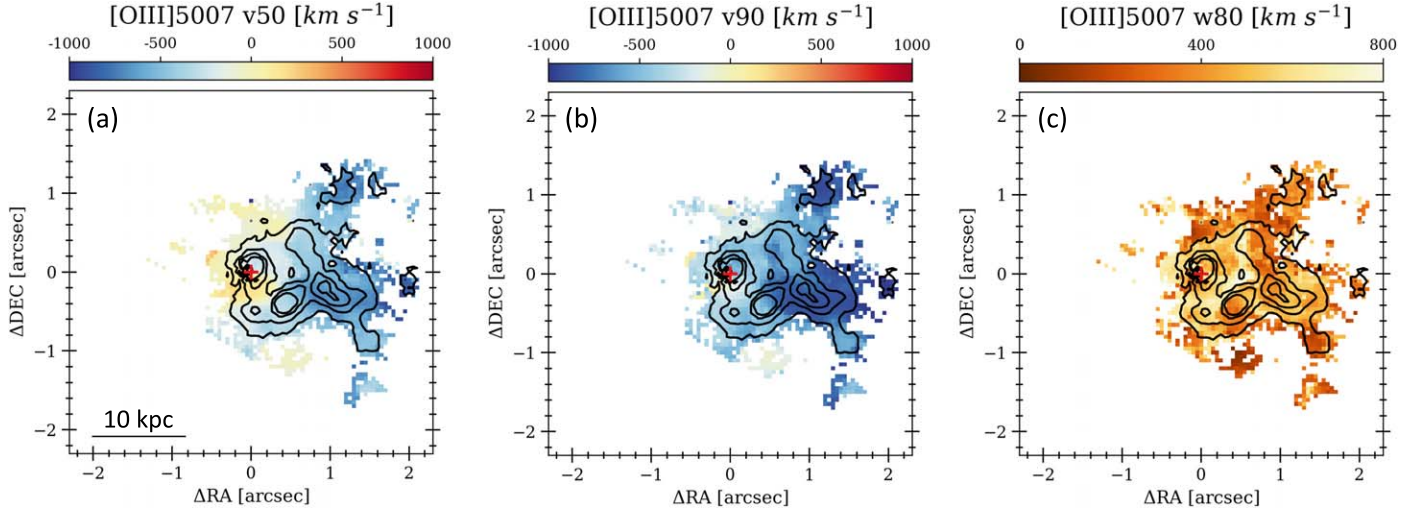


Figure 4. Kinematics of the [O III]-emitting gas in XID 228. (a) 50-percentile (median) velocities, v_{50} , (b) 90-percentile line widths, w_{80} . These images are on the same spatial scale and orientation as Figures 2(a) and (b). The black contours trace the blueshifted [O III] 5007 emission shown in Figure 3(a). Note the general lack of gas with positive velocities on large scale in panels (a) and (b), and the north–south gradient within the central arcsecond region ($R \lesssim 4$ kpc) in panel (a) due to rotational motion in the host galaxy.

results (Section 5.1), and we also reassess the evidence for negative and positive feedback in this system (Section 5.2).

5.1. Energetics of the [O III] Outflow

The [O III] $\lambda 5007$ emission line is by far the brightest line emitted by the outflow within the rest-frame visible range covered by the NIRSpc data cube. It is also well separated in wavelength from neighboring emission lines in contrast to $H\alpha$, which is blended with [N II] 6548, 6583. Finally, this forbidden line is unaffected by line emission from the central high-density ($n_e > 10^9 \text{ cm}^{-3}$) broad-line region (BLR), while broad-line $H\beta$ and $H\alpha$ are prominent in this type 1 quasar (Figure 1). Therefore, we use the strength of [O III] 5007 rather than that of $H\alpha$ or $H\beta$ to estimate the mass of the outflowing gas (Cano-Díaz et al. 2012; Veilleux et al. 2020):

$$M_{\text{ionized}} = 5.3 \times 10^8 \frac{C_e L_{44}([\text{O III } 5007])}{n_{e,2} 10^{[\text{O/H}]}} M_{\odot}, \quad (1)$$

where $L_{44}([\text{O III } 5007])$ is the luminosity of [O III] $\lambda 5007$, normalized to $10^{44} \text{ erg s}^{-1}$, $n_{e,2}$ is the average electron density, normalized to 10^2 cm^{-3} , $C_e \equiv \langle n_e^2 \rangle / \langle n_e \rangle^2$ is the electron density clumping factor, which can be assumed to be of order unity on a cloud-by-cloud basis (i.e., each cloud has uniform density), and $10^{[\text{O/H}]}$ is the oxygen-to-hydrogen abundance ratio relative to the solar value. The ionized mass derived from this expression assumes an electron temperature $T \sim 10^4 \text{ K}$ and electron density $n_e \lesssim 7 \times 10^5 \text{ cm}^{-3}$ the critical density associated with the [O III] 5007 transition above which collisional de-excitation becomes significant. The electron density in the extended [O III] nebula is well below this value. We measure $\log ([\text{S II } 6716/6731]) \approx 0.0\text{--}0.1$ in the outflowing portion of the nebula (Figure 7(b)), corresponding to a median electron density of $\sim 410 \text{ cm}^{-3}$. We take the [O III] 5007 line flux, $2.4 \times 10^{-16} \text{ erg s}^{-1} \text{ cm}^{-2}$, in the portion of the extended nebula where the individual Gaussian component(s) have $v_{50} \leq -300 \text{ km s}^{-1}$, which is well in excess of observed velocities due to rotation, to be representative of the outflowing gas in this

object. We assume a solar oxygen abundance in the nebula ($[\text{O/H}] = 0$) and use the median extinction in the outflow of $A_V = 0.52 \text{ mag}$ to derive an extinction-corrected ionized mass $M_{\text{ionized}} = 1 \times 10^7 M_{\odot}$ in the outflow. Note that the oxygen abundance may be higher than solar near the center of this massive galaxy. Meanwhile, up to 40% of the oxygen atoms may be depleted onto dust grains (Baron & Netzer 2019). These two effects may partly cancel each other. The readers should thus be cautious when interpreting the results.

This value of M_{ionized} is nearly two orders of magnitude smaller than the value derived from the observed (not corrected for extinction) $H\beta$ line emission in the ground-based IFS data analyzed by Cresci et al. (2015). A factor of ~ 4 is accounted for by the higher n_e used in our calculations (410 versus 100 cm^{-3}). We have compared our absolute flux measurements with those in the literature and found an excellent agreement to within $\pm 20\%$ of the values published in Scholtz et al. (2020). The outflow mass derived in our data is not sensitive to our adopted definition for the outflow, $v_{50} \leq -300 \text{ km s}^{-1}$. The [O III] flux is boosted by only $\sim 33\%$ if we instead use $v_{50} \leq -200 \text{ km s}^{-1}$ for the outflow threshold. The significant gain in resolution and sensitivity of the NIRSpc IFU over ground-based IFS, combined with our careful removal of the quasar light with `q3dfit`, provides an unprecedented view of the outflow in XID 228 and likely accounts for most of this discrepancy. This is compounded by the fact that the $H\beta$ line used as a mass tracer by Cresci et al. (2015) is more sensitive to errors in the quasar light removal than [O III] 5007 because it is typically an order of magnitude fainter than [O III] 5007 (Figures 6(a), (e)) and lies on top of the quasar broad-line $H\beta$ emission.

To estimate the outflow mass rate and energetics, we need to know the dynamical timescale of each parcel i of outflowing gas, $\tau_{\text{dyn},i} \approx (R_{\text{deproj},i}/v_{\text{deproj},i}) = (R_i/\sin \theta_i)(v_i/\cos \theta_i)^{-1} = (R_i/v_i) \cot(\theta_i)$, where R_i is the measured distance from the center of the gas parcel on the sky, v_i is the measured outflow radial velocity of that same gas parcel, and θ_i is the angle between the outflow velocity of the gas parcel and our line of sight. The integrated mass outflow rate is the sum of $m_i/\tau_{\text{dyn},i}$

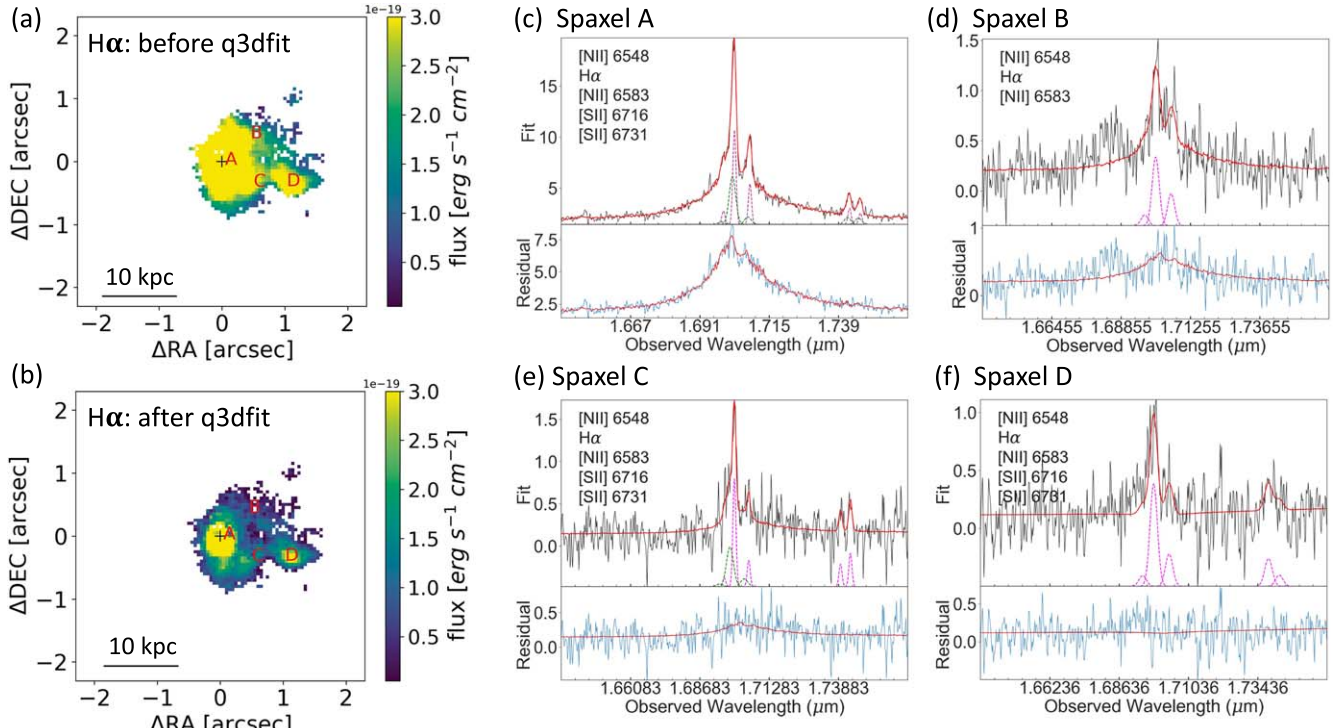


Figure 5. Same as Figure 2 but for the H α spectral region.

over all gas parcels, namely

$$\dot{M} = \sum \dot{m}_i = \sum m_i (v_i/R_i) \tan(\theta_i). \quad (2)$$

The corresponding momenta and kinetic energies and their outflow rates are

$$p = \sum m_i v_i \sec \theta_i, \quad (3)$$

$$\dot{p} = \sum \dot{m}_i v_i \sec \theta_i, \quad (4)$$

$$E = \frac{1}{2} \sum \{m_i [(v_i \sec \theta_i)^2 + 3 \sigma_i^2]\}, \quad (5)$$

$$\dot{E} = \frac{1}{2} \sum \{\dot{m}_i [(v_i \sec \theta_i)^2 + 3 \sigma_i^2]\}, \quad (6)$$

where the energy includes both the bulk kinetic energy due to the outflowing gas and the turbulent kinetic energy (where we assume the same velocity dispersion σ in each dimension).

In the following discussion, we set $v_i = v_{50}$ of the individual Gaussian component(s) in the [O III] line profile at each spaxel where the outflow is detected (following our definition of the outflow, v_{50} must be $\leq -300 \text{ km s}^{-1}$). A derivation of the values of θ_i requires detailed kinematic modeling of the outflow, which is beyond the scope of this first-look paper (W. L. Liu et al. 2023, in preparation). Here, we make a number of simplifying assumptions to estimate the energetics of the outflow. First, we note that most ($\sim 97\%$) of the outflowing gas is in the bright [O III] plume and shows only moderate velocity variations across, and perpendicular to, the plume. This is consistent to first order with a simple kinematic model where all gas parcels in the plume move coherently along the same direction, i.e., $\theta_i = \theta$. The value of θ may be constrained if the absence of the redshifted counterpart to the outflow in our data is due to obscuration by the host galaxy, assuming biconical symmetry with the observed blueshifted outflow. Recall that the outflow extends beyond the bright

plume to trace a cone with an opening angle $\phi \sim 90^\circ$ (Figures 3(a) and 4(b)). The main axis of the cone must therefore be tilted by $\lesssim 45^\circ$ from our line of sight, i.e., $\theta \lesssim 45^\circ$, assuming biconical symmetry and a favorable face-on galaxy orientation. Note, however, that this assumption breaks down if we are dealing with a one-sided outflow. A sketch of the outflow geometry, as seen on the sky, is shown in Figure 8.

Assuming $\theta_i = \theta = 45^\circ$ in Equations (2)–(6), we get $\dot{M} = 1.9 M_\odot \text{ yr}^{-1}$, $\dot{p} = 2.4 \times 10^{34} \text{ dynes}$, and $\dot{E} = 3.6 \times 10^{42} \text{ erg s}^{-1}$. Not surprisingly, these outflow mass rate and energetics are two orders of magnitude smaller than the values derived from the ground-based IFS data (Cresci et al. 2015). This difference is due to the $\sim 100\times$ smaller outflowing ionized gas mass in the NIRSpec data rather than to our simplifying assumption that the outflow is largely along $\theta = 45^\circ$. Under this simple assumption, the dynamical timescale of the outflowing gas ranges from $\lesssim 0.1 \text{ Myr}$ nearest the quasar to $\gtrsim 10 \text{ Myr}$ at 17 kpc from the quasar. In an independent analysis of the exact same Q3D NIRSpec data cube on XID 228, Cresci et al. (2023) recently reported [O III]-based outflow mass rate and energetics that agree within the errors (factor of ~ 3) with the values reported here.

The radiative pressure due to the AGN, $L_{\text{AGN}}/c \approx 7 \times 10^{35} \text{ dynes}$ (where we used $L_{\text{AGN}} \sim 2 \times 10^{46} \text{ erg s}^{-1}$, derived from the spectral energy distribution decomposition of Lusso et al. 2012), is $35\times$ larger than the measured momentum rate \dot{p} in the outflow. The quasar can thus in principle easily drive this outflow via radiation pressure. In the single-scattering optically thin limit, the momentum flux imparted onto the gas is simply $L_{\text{absorbed}}/c \simeq (1 - e^{-\tau_{\text{UV}}})L_{\text{AGN}}/c$, where τ_{UV} is the optical depth to the UV radiation. Dust in the outflowing gas (Figure 7(a)) will boost this term significantly.

The ratio of the kinetic energy outflow rate to the AGN luminosity in this object, $\dot{E}/L_{\text{AGN}} = 1.8 \times 10^{-4}$, is low but not unusually so for a type 1 quasar with this luminosity (e.g.,

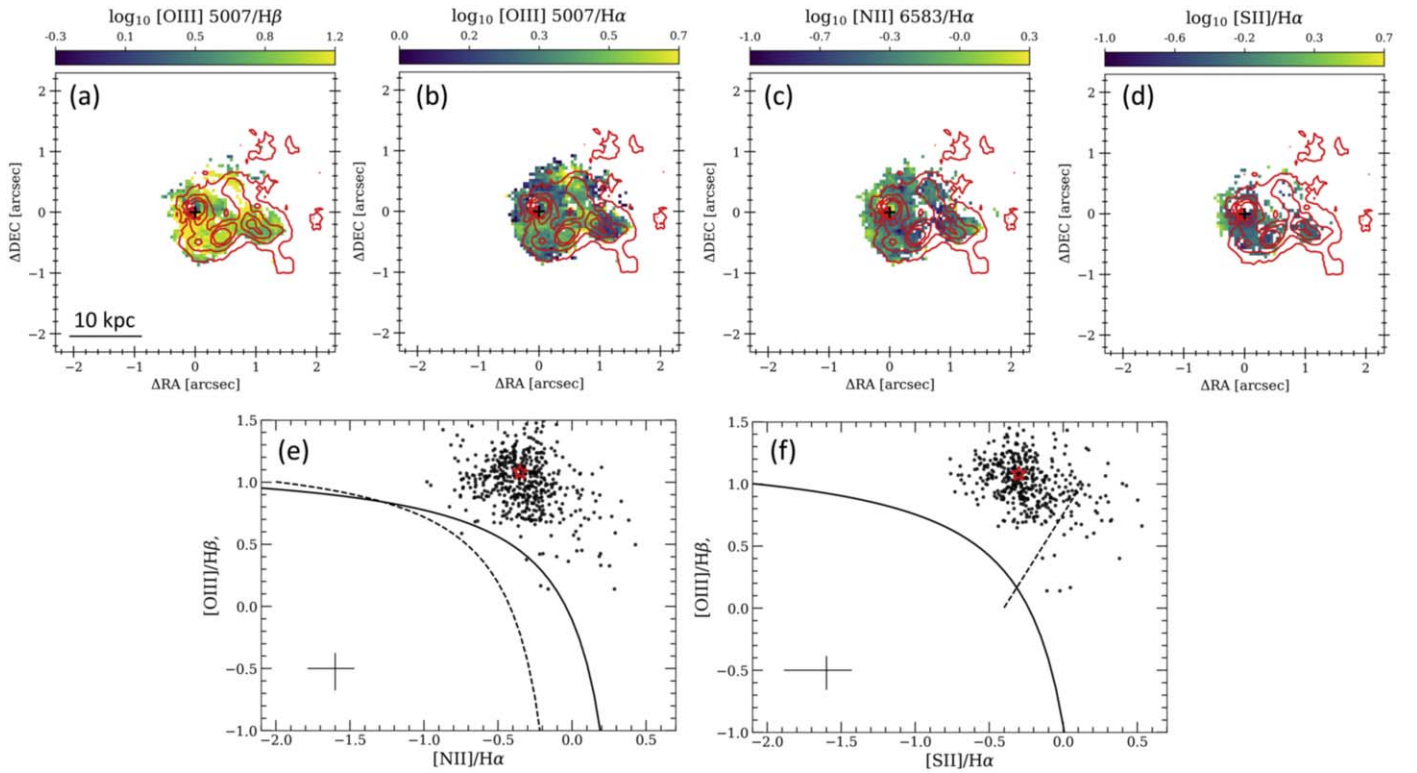


Figure 6. In the top panels we show the line ratio maps of the extranuclear line emission in XID 2028: (a) [O III] 5007/H β , (b) [O III] 5007/H α , (c) [N II] 6583 \AA /H α , and (d) [S II] 6716, 6731/H α . These images are on the same spatial scale and orientation as Figure 2(a). The red contours trace the blueshifted [O III] 5007 emission shown in Figure 3(a). The bottom panels are the BPT (e) and VO87 (f) diagnostic line ratio diagrams derived from these maps. The typical uncertainties on the line ratios are indicated in the bottom-left corner of these diagrams. These results are derived from the simultaneous q3dfit analysis of the extranuclear H β , [O III] 4959, 5007 \AA , H α , [N II] 6548, 6583 \AA , and [S II] 6716, 6731 \AA line emission. See text for more details. In both panels, the black lines are the theoretical curves separating AGN (above right) and star-forming galaxies (below left) from Kewley et al. (2001). The dashed line in panel (e) is the empirical curve from Kauffmann et al. (2003) showing the same separation. As discussed in the text, the line ratios in both diagrams are consistent with photoionization by the central quasar ($D_{\text{AGN}} = 0.70-1$).

Fiore et al. 2017; Rupke et al. 2017; Harrison et al. 2018). Recently, a weak, loosely collimated, radio jet has been purported to exist in XID 2028 (source #10964 in Figure 6 of Vardoulaki et al. 2019). The radio emission is roughly aligned along the same southwestward direction, and extends on a similar scale as the brightest blueshifted [O III] line-emitting cloud in Figure 3(a). This loose jet may contribute to driving the observed outflow or may be the by-product of shocks produced where the fast outflowing material collides with the ambient host ISM (e.g., Whittle et al. 1988; Whittle 1992; Zakamska & Greene 2014).

Note that the mass outflow rate is much smaller than the dust-obscured star formation rate in XID 2028, $\text{SFR} = 134^{+132}_{-70} M_{\odot} \text{ yr}^{-1}$, inferred from the ALMA observations in the rest-frame far-IR by Scholtz et al. (2020), adjusted to our cosmology, assuming that the AGN does not contribute to the far-IR fluxes. Since the implied mass-loading factor, \dot{M}/SFR , is much smaller than unity, we cannot formally rule out the possibility that stellar processes, rather than the quasar itself, drive this outflow. Indeed, the energy rate from a starburst with $\text{SFR} = 134 M_{\odot} \text{ yr}^{-1}$ is $\dot{E}_{*} \approx 7 \times 10^{41} \text{ SFR erg s}^{-1} = 1 \times 10^{44} \text{ erg s}^{-1}$ (e.g., Veilleux et al. 2005), or $\sim 30\times$ larger than the measured kinetic power \dot{E} in the outflow. While the maximum outflow velocity in XID 2028, $\sim 1000 \text{ km s}^{-1}$, is large in comparison to those of local starburst-driven winds, it is not exceptionally high for more distant compact starburst galaxies such as XID 2028 (e.g., Tremonti et al. 2007; Rupke et al. 2019).

5.2. Impact of the Quasar and Outflow on the Host Galaxy

As discussed in Section 4.3, the optical line ratios in the extended nebula of XID 2028 are consistent with those expected for AGN photoionization ($D_{\text{AGN}} = 0.70-1$). Thus, hot and young stars, if present in the host galaxy, do not contribute significantly to the ionization of the warm ionized gas probed by the optical lines. This statement seems to be inconsistent with the large star formation rate ($\text{SFR} = 134 M_{\odot} \text{ yr}^{-1}$) derived by Brusa et al. (2018) and Scholtz et al. (2020) using the rest-frame far-IR flux from ALMA. Barring contamination of the far-IR flux by AGN continuum emission, most of the star formation activity in XID 2028 must therefore be shrouded in dust to make it undetectable in the rest-frame optical band.²⁷ This seems plausible given that XID 2028 is the prototypical obscured quasar selected from the Cosmic Origins Survey (COSMOS) survey based on its observed red color ($r - K = 4.81$) and high X-ray to optical flux ratio (Hasinger et al. 2007; Brusa et al. 2018). Indeed, the host of XID 2028 has a large (dusty) molecular gas mass of $\sim 1 \times 10^{10} M_{\odot}$ (Brusa et al. 2018). The obscured star formation distribution in this object, traced by the ALMA high-resolution 1.3-mm (rest-frame 500 μm) flux map presented in Brusa et al. (2018) (see also Scholtz et al. 2020), is remarkably symmetric around the quasar except for a narrow plume of emission that juts out $\sim 1''.1$

²⁷ For comparison, we derive an upper limit of $\text{SFR} = 25 M_{\odot} \text{ yr}^{-1}$ from the total H α flux in the nebula using the $\text{SFR}-L_{\text{H}\alpha}$ relation from Kennicutt & Evans (2012).

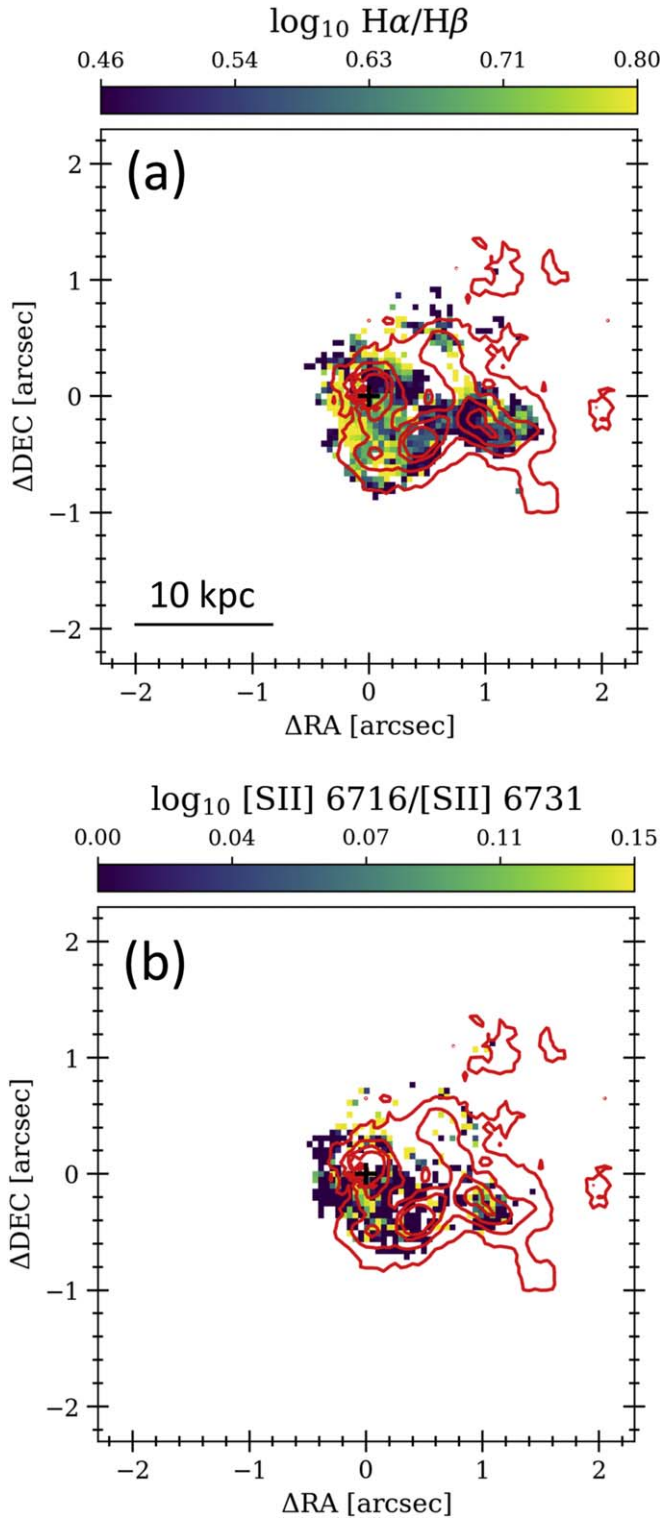


Figure 7. Maps of (a) $H\alpha/H\beta$ line ratio, an indicator of dust reddening and extinction and (b) $[SII] 6716/6731$ line ratio, an indicator of the electron density, in the extended nebula around XID 2028. These images are on the same spatial scale and orientation as Figure 1(a). The red contours trace the blueshifted $[O III] 5007$ emission shown in Figure 3(a).

(~ 9 kpc) in the northeast direction ($PA \approx 45^\circ$). Faint $[O III] 5007$ line emission at near-systemic velocity is detected in this general direction (Figure 3(b)) but no other emission lines lie above the detection limit in our data (Figures 4(a)–(d)), and so the dominant source of ionization of the gas responsible for this

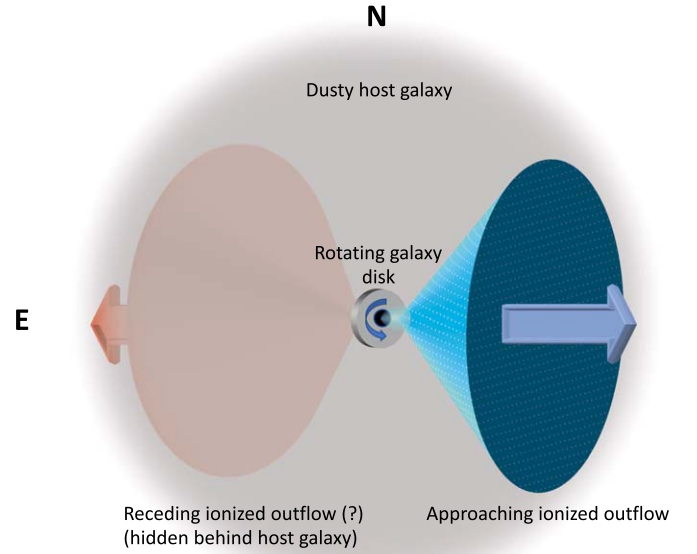


Figure 8. Geometry of the warm ionized outflow traced by $[O III]$ and $H\alpha$ in XID 2028, as seen on the sky. The western plume of outflowing material lies inside of a wider conical outflow with an opening angle $\phi \sim 90^\circ$ (shown in blue to indicate approaching material along our line of sight). There is no evidence in the NIRSpc data cube for the receding outflow cone (shown in red). This cone is either absent in $[O III]$ and $H\alpha$ or hidden by the dusty host galaxy. If hidden, then the approaching outflow cone must be tilted by $\lesssim 45^\circ$ from our line of sight, i.e., $\theta \lesssim 45^\circ$, to avoid detection of the receding outflow east of the quasar, assuming biconical symmetry and a favorable face-on galaxy orientation. The kinematics of the ionized gas in the inner arcsecond ($R \lesssim 4$ kpc) are dominated by rotation from the host galaxy.

faint $[O III]$ emission cannot be constrained from the optical line ratios.

Given the crucial role played by the dust in shaping our views of XID 2028, it may be surprising to realize that this object is a relatively bright source in the rest-frame near-UV (NUV; $\sim 3000 \text{ \AA}$). Following Brusa et al. (2010, their Figure 13), Cresci et al. (2015, their Figure 4), and Scholtz et al. (2020, their Figure 11), we compare the extent of the outflow traced by the blueshifted $[O III]$ line emission shown in Figure 3(a) with the archival HST/ACS F814W image that was obtained as part of COSMOS (Scoville et al. 2007). Figure 9 shows a clear asymmetry of the NUV emission in the general direction of the outflow. Some of the extended NUV emission roughly coincides with the brighter $[O III]$ clouds in the outflowing plume of gas, while other NUV emission loosely follow the fainter wide-angle cone of outflowing $[O III]$ -emitting material.

The NUV emission is often used as a star formation indicator in unobscured regions of galaxies (e.g., Kennicutt & Evans 2012). Taken at face, the flux of the extended NUV emission beyond $r = 0''.05$, $\sim 7 \times 10^{-16} \text{ erg s}^{-1} \text{ cm}^{-2}$, translates into a star formation rate $SFR_{NUV} \sim 1 M_\odot \text{ yr}^{-1}$, which may be considered an upper limit on the rate of (unobscured) star formation triggered by the outflow as it propagates through the host ISM (positive feedback). However, the AGN-like line ratios in this region are inconsistent with this interpretation of the NUV emission. Moreover, this interpretation is fraught with errors when dealing with dusty systems such as XID 2028, especially around intense sources of UV radiation such as quasars. Extended NUV emission has been detected in several luminous obscured quasars, tracing giant

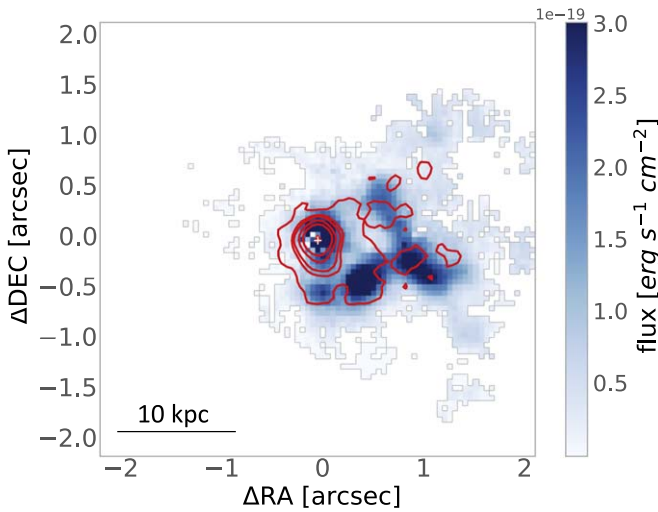


Figure 9. Comparison of the blueshifted (< -300 km s $^{-1}$) [O III] line emission (same as Figure 3(a)) with the rest-frame NUV (~ 3000 Å) continuum emission in the HST/ACS F814W image (red contours). Note the western asymmetry of the NUV emission in the direction of the [O III] outflow, which is consistent with a scattering cone.

scattering cones where the quasar radiation field is scattered off dust in the surrounding material, confirmed by spectropolarimetric data (Zakamska et al. 2006; Obied et al. 2016; Wylezalek et al. 2016). About 75% of the observed flux at ~ 3000 Å in luminous obscured quasars may be due to scattered light, which if left unaccounted for may strongly bias estimates of the star formation rates of quasar hosts.

An analysis of the rest-frame NUV emission in the first target of the Q3D JWST ERS program, J1652, revealed a giant scattering cone along the direction of the outflow in this quasar (Wylezalek et al. 2022). Given the presence of dust in the outflowing gas of XID 2028 (Figure 7(a)) and the loose connection between this gas and the rest-frame NUV emission (Figure 9), we argue that the same scattering process is taking place in this object. The loose spatial correlation of the extended NUV emission with the wind-angle conical outflow of XID 2028 is reminiscent of other scattering cones in starburst-driven winds (e.g., M82; Hoopes et al. 2005) and quasar-driven winds (Zakamska et al. 2006; Obied et al. 2016; Wylezalek et al. 2016). Contrary to the [O III] emission that traces n_e^2 , the spatial distribution of the scattered NUV light is a complex function of several variables (e.g., geometry and strength of the NUV radiation field, location, and dust column density distribution of the scattering material, and our viewing angle with respect to this material). Consequently, this loose correlation between NUV emission and the [O III] clouds is actually expected.

The absence of a tight one-to-one correlation between the extended NUV emission and brightest [O III] 5007 clouds also rules out the possibility that the extended NUV emission is entirely due to [Ne V] 3426 and Mg II 2800 line emission within the F814W filter bandpass (~ 7000 – 9500 Å or ~ 2700 – 3650 Å in the rest frame; note that [O II] 3727 lies outside of the bandpass). This is confirmed quantitatively: the AGN photoionization models of Groves et al. (2004) predict fluxes for ([Ne V] 3426 + Mg II 2800) that are $\lesssim 25\%$ of the [O III] 5007 fluxes in cases where [O III] 5007/H $\beta \approx 10$ as seen in the outflow (Figure 6). Dust extinction in the outflowing material ($A_V = 0.5$ mag) will reduce the strength of [Ne V] 3426 + Mg II 2800 relative to [O III] 5007 by a factor of ~ 2 . In the end, we find that the [Ne V]

3426 + Mg II 2800 line emission contributes at most $\sim 10\%$ of the observed extended NUV emission.

Overall, the JWST and HST data paint a picture of XID 2028 in a blow-out phase where the combined action of radiative and mechanical modes of quasar feedback have accelerated warm ionized gas up to high velocities, breaking through the thick dusty shroud of the obscured quasar. While the bulk ($\sim 97\%$) of the outflowing material lies in a loosely collimated plume west of the quasar, fainter outflowing clouds trace a wider cone centered on the plume spanning an angle $\phi \sim 90^\circ$. The intense radiation field from the quasar is ionizing and possibly also driving the warm ionized outflow out to at least 17 kpc. The lack of ionization edges in the outflow line-emitting nebula indicates that it forms a matter-bounded structure where some of the ionizing radiation manages to escape the host galaxy and may potentially ionize the surrounding CGM, keeping it warm and perhaps preventing cold gas from accreting back onto the galaxy and forming new stars.

The outflow rate of $1.9 M_\odot$ yr $^{-1}$ derived from our analysis of the [O III] nebula is small for such a powerful quasar (e.g., Cano-Díaz et al. 2012; Fiore et al. 2017; Rupke et al. 2017). It is also much smaller than the cold-gas mass outflow rate reported by Brusa et al. (2018), 50 – $350 M_\odot$ yr $^{-1}$, based on a tentative ($< 5\sigma$) detection of high-velocity CO gas with ALMA and a CO-to-H $_2$ conversion factor $\alpha_{\text{CO}} = 0.13$ – $0.80 M_\odot / (\text{K km s}^{-1} \text{ pc}^2)$. The neutral-gas outflow traced by the broad Na I D absorption feature in the spectrum of XID 2028 (Figure 1) is spatially unresolved in the JWST data ($r \lesssim 1$ kpc), so the neutral-gas mass outflow rate remains unconstrained (as is the case of the neutral/low-ionization Mg II 2800 outflow detected by Perna et al. 2015). Given the median outflow velocity in the [O III]-emitting material ($v_{50} \approx 550$ km s $^{-1}$ for the entire line profile) and estimated stellar mass of $\log M_*/M_\odot = 11.65^{+0.35}_{-0.35}$ from Brusa et al. (2018), the escape fraction²⁸ of the warm ionized gas is $\sim 3\%$, so only $0.06 M_\odot$ yr $^{-1}$ is able to escape the galaxy potential and make it to the IGM. This warm ionized outflow event is thus a negligible contributor to the enrichment of the CGM, let alone the IGM. The neutral- and cold-gas outflows of XID 2028 have lower velocities and smaller sizes than the [O III] outflow, so they will also not contribute to the enrichment of the CGM and IGM.

Under these circumstances, the unusually small molecular gas fraction in XID 2028 that was reported by Brusa et al. (2018; a ratio of molecular gas to stellar mass $\lesssim 5\%$, significantly smaller than those typically measured in high- z galaxies with similar specific star formation rates) is hard to explain as due purely to ejective quasar mechanical feedback. We instead favor joint action of radiative and mechanical feedback where a significant fraction of the quasar hard ionizing radiation is able to escape through the cone created by the wide-angle outflow, dissociating/ionizing the molecular gas on its path.

In this scenario, the quasar radiation field may only affect the gas within the outflow (bi)cone.²⁹ Assuming a simple (bi)conical symmetry for the outflow, the solid angle subtended by the

²⁸ This is the fraction of warm ionized gas in the outflow that has a velocity above the local escape velocity of the galaxy (Veilleux et al. 2020): $v_{\text{esc}}(r) = v_{\text{circ}} \sqrt{2 [1 + \ln(r_{\text{max}}/r)]} \approx 1000$ km s $^{-1}$, where we replaced the circular velocity with $\sqrt{2S}$ using $\log S = 0.29 \log M_* - 0.93$, and used $r = 10$ – 20 kpc and $r_{\text{max}} = 100$ – 300 kpc, the maximum radius of the galaxy (which is assumed to be an isothermal sphere with truncation radius r_{max}).

²⁹ Recall that the redshifted counterpart to the conical outflow is not detected in the JWST data but it may be hidden from view by the intervening dusty host galaxy.

outflow, normalized to 4π steradians, is $(1 - \cos \phi/2) \times 50\%$ ($100\% = 15\%$ (30%)). If the galaxy ISM and CGM are, to first order, distributed spherically symmetrically around the quasar, then only about 15% (30%) of this gas may be affected by the quasar ionizing radiation. This fraction may be less in the case of the molecular disk in the inner arcsecond (Brusa et al. 2018). This may explain why this object lies on the main sequence of star-forming galaxies at $z \approx 2$ (Brusa et al. 2018). In the end, we find no convincing evidence for star formation quenching by quasar mechanical or radiative feedback in this object.

6. Conclusions

We obtained NIRSpect integral-field spectroscopic data of the $z = 1.593$ obscured quasar XID 2028 as part of the Q3D Early Release Science program. The data were carefully analyzed using `q3dfit`, which is a dedicated software package for the removal of bright point-spread functions from JWST data cubes. The main results of this analysis are as follows.

1. *Outflow morphology.* The exquisite sensitivity, angular resolution, and quality of the PSF characterization of the NIRSpect data reveal a highly structured one-sided plume of fast outflowing [O III] line-emitting gas surrounded by fainter and slightly slower outflowing clouds distributed in a cone that subtends an angle $\sim 90^\circ$.
2. *Outflow kinematics and dynamics.* The outflow completely dominates the kinematics of the extended line-emitting nebula, except for the inner arcsecond ($R \lesssim 4$ kpc) region where a north-south velocity gradient is present, reflecting rotational motion in the host galaxy. The warm ionized outflow is characterized by high velocities of up to 1000 km s^{-1} (90-percentile) but very little mass ($\sim 10^7 M_\odot$), resulting in modest outflow energetics with mass, momentum, and kinetic energy outflow rates of $\dot{M} = 1.9 M_\odot \text{ yr}^{-1}$, $\dot{p} = 2.4 \times 10^{34} \text{ dynes}$, and $\dot{E} = 3.6 \times 10^{42} \text{ erg s}^{-1}$, respectively. Radiation pressure by the luminous quasar can easily drive this dusty outflow, although a starburst-driven origin to this outflow cannot be formally ruled out if the rest-frame far-IR flux derived from ALMA data is a reliable indicator of the (obscured) star formation rate in this system.
3. *Impact of the quasar and outflow on the host galaxy.* Photoionization by the quasar dominates throughout the nebula, despite the large obscured star formation rate inferred from the far-IR. The rest-frame NUV ($\sim 3000 \text{ \AA}$) emission from an archival HST/F814W image shows a clear asymmetry in the direction of the outflow consistent with a giant scattering cone where the NUV emission from the quasar is scattered by dust in the outflowing gas. Overall, quasar mechanical feedback likely does not directly influence the star formation rate in the host galaxy of XID 2028, neither negatively nor positively. However, radiative feedback by the quasar radiation field, aided by the clearing of the gas by the outflow, may heat and dissociate/ionize 15%–30% of the surrounding ISM and CGM, and prevent this gas from raining back down and forming new stars.

Our use of the NIRSpect rest-frame optical IFS data to study obscured quasar XID 2028 limits our view of the outflow and surrounding host galaxy to regions with $A_V \lesssim 3\text{--}5$ mag. An analysis of the Q3D MIRI/MRS IFS data on this object should

shed new light on obscured star formation in this system, and on the roles that the large-scale outflow and quasar radiation field play, if any, in reducing the molecular gas fraction in this system, as well as quenching or boosting star formation activity on local (ISM) and global (CGM) scales.

Acknowledgments

S.V., W.L., A.V., D.S.N.R., and N.L.Z. were supported in part by NASA through STScI grant No. JWST-ERS-01335. N. L.Z. further acknowledges support by the Institute for Advanced Study through J. Robert Oppenheimer Visiting Professorship and the Bershadsky Fund. D.W. and C.B. acknowledge support through an Emmy Noether Grant of the German Research Foundation, a stipend by the Daimler and Benz Foundation and a Verbundforschung grant by the German Space Agency. J.B.-B. acknowledges support from grant IA-101522 (DGAPA-PAPIIT, UNAM) and funding from the CONACYT grant CF19-39578. The data products are available from the corresponding author upon appropriate request.

Facilities: JWST(NIRSpect), HST(WFC3).

Software: astropy (Astropy Collaboration et al. 2013, 2018), JWST Calibration Pipeline (Version 1.8.4) (Bushouse et al. 2022), `q3dfit` (D. S. N. Rupke et al. 2023, in preparation).

ORCID iDs

Sylvain Veilleux  <https://orcid.org/0000-0002-3158-6820>
 Weizhe Liu  <https://orcid.org/0000-0003-3762-7344>
 Andrey Vayner  <https://orcid.org/0000-0002-0710-3729>
 Dominika Wylezalek  <https://orcid.org/0000-0003-2212-6045>
 David S. N. Rupke  <https://orcid.org/0000-0002-1608-7564>
 Nadia L. Zakamska  <https://orcid.org/0000-0001-6100-6869>
 Yuzo Ishikawa  <https://orcid.org/0000-0001-7572-5231>
 Caroline Bertemes  <https://orcid.org/0000-0002-6948-1485>
 Jorge K. Barrera-Ballesteros  <https://orcid.org/0000-0003-2405-7258>
 Hsiao-Wen Chen  <https://orcid.org/0000-0001-8813-4182>
 Nadiia Diachenko  <https://orcid.org/0009-0003-5128-2159>
 Andy D. Goulding  <https://orcid.org/0000-0003-4700-663X>
 Jenny E. Greene  <https://orcid.org/0000-0002-5612-3427>
 Kevin N. Hainline  <https://orcid.org/0000-0003-4565-8239>
 Timothy Heckman  <https://orcid.org/0000-0001-6670-6370>
 Sean D. Johnson  <https://orcid.org/0000-0001-9487-8583>
 Dieter Lutz  <https://orcid.org/0000-0003-0291-9582>
 Nora Lützgendorf  <https://orcid.org/0000-0002-4034-0080>
 Vincenzo Mainieri  <https://orcid.org/0000-0002-1047-9583>
 Roberto Maiolino  <https://orcid.org/0000-0002-4985-3819>
 Nicole P. H. Nesvadba  <https://orcid.org/0000-0001-5783-6544>
 Patrick Ogle  <https://orcid.org/0000-0002-3471-981X>
 Swetha Sankar  <https://orcid.org/0000-0002-4419-8325>
 Eckhard Sturm  <https://orcid.org/0000-0002-0018-3666>

References

- Allen, M. G., Dopita, M. A., Tsvetanov, Z. I., & Sutherland, R. S. 1999, *ApJ*, **511**, 686
 Allen, M. G., Groves, B. A., Dopita, M. A., Sutherland, R. S., & Kewley, L. J. 2008, *ApJS*, **178**, 20
 Arrighi Battaia, F., Hennawi, J. F., Prochaska, J. X., et al. 2019, *MNRAS*, **482**, 3162
 Astropy Collaboration, Robitaille, T. P., Tollerud, E. J., et al. 2013, *A&A*, **558**, A33

- Astropy Collaboration, Price-Whelan, A. M., Sipőcz, B. M., et al. 2018, *AJ*, **156**, 123
- Bajtlik, S., Duncan, R. C., & Ostriker, J. P. 1988, *ApJ*, **327**, 570
- Baldwin, J. A., Phillips, M. M., & Terlevich, R. 1981, *PASP*, **93**, 5
- Baron, D., & Netzer, H. 2019, *MNRAS*, **486**, 4290
- Benson, A. J., Bower, R. G., Frenk, C. S., et al. 2003, *ApJ*, **599**, 38
- Böker, T., Arribas, S., Lützgendorf, N., et al. 2022, *A&A*, **661**, A82
- Borisova, E., Cantalupo, S., Lilly, S. J., et al. 2016, *ApJ*, **831**, 39
- Bruns, L. R., Wyithe, J. S. B., Bland-Hawthorn, J., & Dijkstra, M. 2012, *MNRAS*, **421**, 2543
- Brusa, M., Bongiorno, A., Cresci, G., et al. 2015, *MNRAS*, **446**, 2394
- Brusa, M., Civano, F., Comastri, A., et al. 2010, *ApJ*, **716**, 348
- Brusa, M., Cresci, G., Daddi, E., et al. 2018, *A&A*, **612**, A29
- Bushouse, H., Eisenhamer, J., Dencheva, N., et al. 2022, JWST Calibration Pipeline, v1.8.4, Zenodo, doi:10.5281/zenodo.7325378
- Cano-Díaz, M., Maiolino, R., Marconi, A., et al. 2012, *A&A*, **537**, L8
- Cresci, G., Bland-Hawthorn, J., & Veilleux, S. 2002, *ApJ*, **576**, 745
- Cecil, G., Bland-Hawthorn, J., Veilleux, S., & Filippenko, A. V. 2001, *ApJ*, **555**, 338
- Cicone, C., Severgnini, P., Papadopoulos, P. P., et al. 2018, *ApJ*, **863**, 143
- Cresci, G., Mainieri, V., Brusa, M., et al. 2015, *ApJ*, **799**, 82
- Cresci, G., Tozzi, G., Perna, M., et al. 2023, *A&A*, **672**, A128
- Croft, S., van Breugel, W., de Vries, W., et al. 2006, *ApJ*, **647**, 1040
- Curran, S. J., & Whiting, M. T. 2012, *ApJ*, **759**, 117
- Dasyra, K. M., Bostrom, A. C., Combes, F., & Vlahakis, N. 2015, *ApJ*, **815**, 34
- Dasyra, K. M., Combes, F., Oosterloo, T., et al. 2016, *A&A*, **595**, L7
- Eilers, A.-C., Hennawi, J. F., Decarli, R., et al. 2020, *ApJ*, **900**, 37
- Elbaz, D., Jahnke, K., Pantin, E., Le Borgne, D., & Letawe, G. 2009, *A&A*, **507**, L359
- Fabian, A. C. 2012, *ARA&A*, **50**, 455
- Farina, E. P., Arrigoni-Battaia, F., Costa, T., et al. 2019, *ApJ*, **887**, 196
- Fiore, F., Feruglio, C., Shankar, F., et al. 2017, *A&A*, **601**, A143
- Francis, P. J., & Bland-Hawthorn, J. 2004, *MNRAS*, **353**, 301
- Gallagher, R., Maiolino, R., Belfiore, F., et al. 2019, *MNRAS*, **485**, 3409
- Gardner, J. P., Mather, J. C., Clampin, M., et al. 2006, *SSRv*, **123**, 485
- Gebhardt, K., Bender, R., Bower, G., et al. 2000, *ApJL*, **539**, L13
- Gonçalves, T. S., Steidel, C. C., & Pettini, M. 2008, *ApJ*, **676**, 816
- Greene, J. E., Zakamska, N. L., & Smith, P. S. 2012, *ApJ*, **746**, 86
- Groves, B. A., Dopita, M. A., & Sutherland, R. S. 2004, *ApJS*, **153**, 9
- Gültekin, K., Richstone, D. O., Gebhardt, K., et al. 2009, *ApJ*, **698**, 198
- Harrison, C. M., Costa, T., Tadhunter, C. N., et al. 2018, *NatAs*, **2**, 198
- Hasinger, G., Cappelluti, N., Brunner, H., et al. 2007, *ApJS*, **172**, 29
- Helton, J. M., Johnson, S. D., Greene, J. E., & Chen, H.-W. 2021, *MNRAS*, **505**, 5497
- Hinkle, J. T., Veilleux, S., & Rupke, D. S. N. 2019, *ApJ*, **881**, 31
- Hoopes, C. G., Heckman, T. M., Strickland, D. K., et al. 2005, *ApJL*, **619**, L99
- Hopkins, P. F., Torrey, P., Faucher-Giguère, C.-A., Quataert, E., & Murray, N. 2016, *MNRAS*, **458**, 816
- Howell, J. H., Mazzarella, J. M., Chan, B. H. P., et al. 2007, *AJ*, **134**, 2086
- Jakobsen, P., Ferruit, P., Alves de Oliveira, C., et al. 2022, *A&A*, **661**, A80
- Johnson, S. D., Chen, H.-W., Straka, L. A., et al. 2018, *ApJL*, **869**, L1
- Kassin, S. A., Weiner, B. J., Faber, S. M., et al. 2007, *ApJL*, **660**, L35
- Kauffmann, G., Heckman, T. M., Tremonti, C., et al. 2003, *MNRAS*, **346**, 1055
- Kennicutt, R. C., & Evans, N. J. 2012, *ARA&A*, **50**, 531
- Kewley, L. J., Dopita, M. A., Sutherland, R. S., Heisler, C. A., & Trevena, J. 2001, *ApJ*, **556**, 121
- Koudmani, S., Henden, N. A., & Sijacki, D. 2021, *MNRAS*, **503**, 3568
- Koudmani, S., Sijacki, D., Bourne, M. A., & Smith, M. C. 2019, *MNRAS*, **484**, 2047
- Koudmani, S., Sijacki, D., & Smith, M. C. 2022, *MNRAS*, **516**, 2112
- Kreimeyer, K., & Veilleux, S. 2013, *ApJL*, **772**, L11
- Li, J., Emonts, B. H. C., Cai, Z., et al. 2021, *ApJL*, **922**, L29
- Liu, W., Veilleux, S., Canalizo, G., et al. 2020, *ApJ*, **905**, 166
- Lusso, E., Comastri, A., Simmons, B. D., et al. 2012, *MNRAS*, **425**, 623
- Maiolino, R., Russell, H. R., Fabian, A. C., et al. 2017, *Natur*, **544**, 202
- Manzano-King, C. M., Canalizo, G., & Sales, L. V. 2019, *ApJ*, **884**, 54
- McNamara, B. R., & Nulsen, P. E. J. 2007, *ARA&A*, **45**, 117
- Morey, K. A., Eilers, A.-C., Davies, F. B., Hennawi, J. F., & Simcoe, R. A. 2021, *ApJ*, **921**, 88
- Nelson, D., Pillepich, A., Springel, V., et al. 2019, *MNRAS*, **490**, 3234
- Nesvadba, N. P. H., Boulanger, F., Salomé, P., et al. 2010, *A&A*, **521**, A65
- Nesvadba, N. P. H., De Breuck, C., Lehnert, M. D., Best, P. N., & Collet, C. 2017, *A&A*, **599**, A123
- Nesvadba, N. P. H., Lehnert, M. D., De Breuck, C., Gilbert, A. M., & van Breugel, W. 2008, *A&A*, **491**, 407
- Nesvadba, N. P. H., Wagner, A. Y., Mukherjee, D., et al. 2021, *A&A*, **654**, A8
- Obied, G., Zakamska, N. L., Wylezalek, D., & Liu, G. 2016, *MNRAS*, **456**, 2861
- Onodera, M., Carollo, C. M., Renzini, A., et al. 2015, *ApJ*, **808**, 161
- Oppenheimer, B. D., Davies, J. J., Crain, R. A., et al. 2020, *MNRAS*, **491**, 2939
- Perna, M., Brusa, M., Cresci, G., et al. 2015, *A&A*, **574**, A82
- Rich, J. A., Kewley, L. J., & Dopita, M. A. 2011, *ApJ*, **734**, 87
- Rich, J. A., Kewley, L. J., & Dopita, M. A. 2014, *ApJL*, **781**, L12
- Rich, J. A., Kewley, L. J., & Dopita, M. A. 2015, *ApJS*, **221**, 28
- Rodríguez del Pino, B., Arribas, S., Piqueras López, J., Villar-Martín, M., & Colina, L. 2019, *MNRAS*, **486**, 344
- Rupke, D. 2018, *Galax*, **6**, 138
- Rupke, D. S. N. 2014, IFSFIT: Spectral Fitting for Integral Field Spectrographs, Astrophysics Source Code Library, ascl:1409.005
- Rupke, D. S. N., Coil, A., Geach, J. E., et al. 2019, *Natur*, **574**, 643
- Rupke, D. S. N., Gültekin, K., & Veilleux, S. 2017, *ApJ*, **850**, 40
- Schawinski, K., Urry, C. M., Simmons, B. D., et al. 2014, *MNRAS*, **440**, 889
- Scholtz, J., Harrison, C. M., Rosario, D. J., et al. 2020, *MNRAS*, **492**, 3194
- Scoville, N., Aussel, H., Brusa, M., et al. 2007, *ApJS*, **172**, 1
- Sharp, R. G., & Bland-Hawthorn, J. 2010, *ApJ*, **711**, 818
- Shin, J., Woo, J.-H., Chung, A., et al. 2019, *ApJ*, **881**, 147
- Spilker, J. S., Bezanson, R., Weiner, B. J., Whitaker, K. E., & Williams, C. C. 2019, *ApJ*, **883**, 81
- Tacchella, S., Carollo, C. M., Renzini, A., et al. 2015, *Sci*, **348**, 314
- Tacchella, S., Dekel, A., Carollo, C. M., et al. 2016, *MNRAS*, **458**, 242
- Tremonti, C. A., Moustakas, J., & Diamond-Stanic, A. M. 2007, *ApJL*, **663**, L77
- Tumlinson, J., Peebles, M. S., & Werk, J. K. 2017, *ARA&A*, **55**, 389
- Vardoulaki, E., Jiménez Andrade, E. F., Karim, A., et al. 2019, *A&A*, **627**, A142
- Vayner, A., Zakamska, N. L., Ishikawa, Y., et al. 2023, *ApJ*, in press
- Veilleux, S., Cecil, G., Bland-Hawthorn, J., et al. 1994, *ApJ*, **433**, 48
- Veilleux, S., Cecil, G., & Bland-Hawthorn, J. 2005, *ARA&A*, **43**, 769
- Veilleux, S., Kim, D. C., Sanders, D. B., Mazzarella, J. M., & Soifer, B. T. 1995, *ApJS*, **98**, 171
- Veilleux, S., Maiolino, R., Bolatto, A. D., & Aalto, S. 2020, *A&ARv*, **28**, 2
- Veilleux, S., & Osterbrock, D. E. 1987, *ApJS*, **63**, 295
- Veilleux, S., Shopbell, P. L., & Miller, S. T. 2001, *AJ*, **121**, 198
- Weiner, B. J., Willmer, C. N. A., Faber, S. M., et al. 2006, *ApJ*, **653**, 1027
- Whittle, M. 1992, *ApJS*, **79**, 49
- Whittle, M., Pedlar, A., Meurs, E. J. A., et al. 1988, *ApJ*, **326**, 125
- Wylezalek, D., Vayner, A., Rupke, D. S. N., et al. 2022, *ApJL*, **940**, L7
- Wylezalek, D., Zakamska, N. L., Liu, G., & Obied, G. 2016, *MNRAS*, **457**, 745
- Yuan, F., & Narayan, R. 2014, *ARA&A*, **52**, 529
- Yuan, T. T., Kewley, L. J., & Sanders, D. B. 2010, *ApJ*, **709**, 884
- Zakamska, N. L., & Greene, J. E. 2014, *MNRAS*, **442**, 784
- Zakamska, N. L., Strauss, M. A., Krolik, J. H., et al. 2006, *AJ*, **132**, 1496